

Condensation formation by impulsive heating in prominences

J. T. Karpen and S. K. Antiochos

*E. O. Hulburt Center for Space Research, Naval Research Laboratory, Washington, DC,
20375-5352*

`judy.karpen@nrl.navy.mil`

ABSTRACT

Our thermal nonequilibrium model for prominence formation provides an explanation for the well-observed presence of predominantly dynamic, cool, dense, material suspended in the corona above filament channels. According to this model, condensations form readily along long, low-lying magnetic field lines when heating is localized near the chromosphere. Often this process yields a dynamic cycle in which condensations repetitively form, stream along the field, and ultimately disappear by falling onto the nearest footpoint. Our previous studies employed only steady heating, as is consistent with some coronal observations, but many coronal heating models predict transient episodes of localized energy release (*e.g.*, nanoflares). Here we present the results of a numerical investigation of impulsive heating in a model prominence flux tube and compare the outcome with previous steady-heating simulations. We find that condensations form readily when the average interval between heating events is less than the coronal radiative loss time (~ 2000 s). As the average interval between pulses decreases, the plasma evolution more closely resembles the steady heating case. The heating scale and presence or absence of background heating also determine whether or not condensations form and how they evolve. Random impulsive heating also forces the condensations to move erratically at speeds comparable to those of discrete moving features observed in prominences, thus accounting for both counterstreaming and higher-speed motions. Our results place important constraints on coronal heating in filament channels, and strengthen the case for thermal nonequilibrium as the process responsible for the plasma structure in prominences.

Subject headings: Sun: prominences — Sun: magnetic fields — Sun: corona

1. Introduction

Recent observations by the Solar and Heliospheric Observatory (SOHO), Transition Region and Coronal Explorer (TRACE), the Swedish Vacuum Solar Telescope (SVST), the Very High Angular Resolution Ultraviolet Telescope (VAULT), and Hinode reveal fine-scale counterstreaming flows and proper motions, and much more spatial and temporal complexity than previously detected in prominences. The overwhelming impression left by these detailed observations is that the bulk of the prominence mass is in the form of transient, moving knots and longer horizontal threads that condense *in situ* in the corona.

The thermal nonequilibrium model for prominence condensations, which we have explored extensively through theoretical analysis and 1D numerical simulations, predicts observable signatures such as the thermal properties, velocity, and mass of moving features in long low-lying flux tubes typical of the core of filament channels. Thermal nonequilibrium is the catastrophic and dynamic consequence of an imbalance among the energy sources and sinks in coronal plasmas within flux tubes longer than ~ 8 times the heating deposition scale (Serio *et al.* 1981; Mok *et al.* 1990; Antiochos & Klimchuk 1991; Dahlburg, Antiochos, & Klimchuk 1998; Antiochos *et al.* 1999). In our investigations of this process, we found that condensations form readily along long, low-lying magnetic field lines when the heating is localized near the chromosphere, as is consistent with several coronal-loop analyses (*e.g.*, Aschwanden, Schrijver, & Alexander 2001; Schmieder *et al.* 2004). We explored thermal nonequilibrium in a range of flux-tube geometries characteristic of filament channels, all with steady heating localized within 1-10 Mm above the base of the corona (Antiochos, MacNeice, & Spicer 2000; Karpen *et al.* 2001, 2003, 2005, 2006).

In the present work, we determine the response of this process to a temporally varying heating rate, as predicted by many coronal heating models (see, *e.g.*, Klimchuk 2006). Assuming a uniform random distribution of pulse onset times, we examine the effects of varying the duration of the heating pulse, the average interval between heating events, and the heating deposition scale. We also investigate the influence of uniform background heating, as assumed in our earlier simulations and in models of thermal nonequilibrium in coronal loops (Müller, Hansteen, & Peter 2003; Müller *et al.* 2005; Mendoza-Briceño *et al.* 2005). We find that impulsive heating produces condensations in most cases. In contrast to the steady-heating runs, however, impulsive heating induces large flows in the system that not only delay the condensation process but also affect the location, instantaneous size, and motion of each condensation. The speed range and erratic movements of the model condensations reproduce the observed mix of counterstreaming and unidirectional flows in prominences.

2. Numerical Simulations

We performed simulations with ARGOS, our workhorse code that solves the one-dimensional hydrodynamic equations for mass, momentum, and energy with a high-order Godunov method and adaptive mesh refinement (AMR) (for further details of the basic methodology see Antiochos *et al.* 1999; Karpen *et al.* 2005). Table 1 lists the key parameters and characteristic features of the simulations performed for this study, as well as the numbers of the corresponding animations of predicted emission intensities in the electronic edition (see caption to Fig. 3 for details). All calculations ran for 10^5 s of simulated time after the onset of footpoint heating (see below). The same flux tube was used in all cases: the slightly dipped flux tube denoted Loop D in Karpen *et al.* (2006). The flux-tube cross-sectional area is uniform; the length is 404.77 Mm, including two 60-Mm chromospheric-photospheric sections; and the maximum height of the flux tube is 20 Mm above the chromosphere. As in our prior studies, the atmosphere is assumed to be a fully ionized plasma with a minimum temperature of 3×10^4 K. The radiative loss function is tailored to maintain the chromosphere at around 30,000 K (see Karpen *et al.* 2005, for details); below this temperature the solar radiative losses are limited by radiative transfer, which is not included in our model.

As in our earlier investigations, the heating has two components: a spatially localized component at each footpoint that is uniform in the chromosphere and falls off exponentially above with a predetermined scale λ , plus a spatially uniform background heating rate of $Q_0 = 1.5 \times 10^{-4}$ ergs cm $^{-3}$ s $^{-1}$ (see Karpen *et al.* 2001, for details). In all cases, an equilibrium consistent with the canonical scaling laws (Rosner, Tucker, & Vaiana 1978) was established first with only the background heating turned on. Starting at 10^5 s ($t_0 = 0$ in the text and Figures), localized heating of the following form was imposed at each footpoint:

$$Q_e(s) = 0.1 \exp[-(s - s_0)/\lambda]/\lambda \quad (\text{steady heating}) \quad (1)$$

$$Q_e(s, t) = Q_e(s) * f(\delta t) \operatorname{sech}^{20}[(t - t_h)/\delta t] \quad (\text{impulsive heating}), \quad (2)$$

where Q is in units of ergs cm $^{-3}$ s $^{-1}$, s is distance along the flux tube in Mm, s_0 is the position of the top of the chromosphere, $\lambda = 1$ or 5 Mm, t is the time in seconds, t_h is the array of start times for heating events, and δt is the heating pulse width (20 or 200 s). In the steady-heating runs, the footpoint heating was ramped up linearly over a 1000-s interval to avoid startup discontinuities. For the calculations with background heating turned off, the background heating was ramped down linearly in the same manner at the start of the footpoint heating. For the impulsive heating, the array of start times at each footpoint was constructed by generating a set of random numbers (different for each footpoint), normalizing the range so the sum does not exceed the run length (10^5 s) and the median value is either 500 s or 2000 s, and setting the minimum and maximum values to exclude the pulse duration.

Events do not overlap in time at a given footpoint. The amplitude and duration of every pulse is the same for each simulation, but the amplitude is adjusted by the factor $f(\delta t)$ so the total energy input is the same for all runs and equal to that of the earlier steady-heating simulations.

3. Results

3.1. Interpulse interval variation

We chose two test values for the average interval between heating events, $\langle dt \rangle$: one comparable to the coronal radiative cooling time (2000 s), and the other significantly less (500 s) but greater than the larger pulse duration. As expected, the shorter interval yields behavior closer to the steady heating case (Fig. 2) than the longer interval. In a symmetric flux tube geometry with the same energy input at each footpoint, steady heating produces a single condensation that sits around the midpoint and grows monotonically at a rate dependent on the heating scale (compare Figs. 2a and 2c).

The 500-s average interval runs all produced one or more condensations (see Figs. 3 and 5), whereas the 2000-s interval runs only produced condensations when the background heating was turned off (see Figs. 4 and 6). For example, Figures 3a and 4a directly compare runs with the same pulse width (20 s) but different $\langle dt \rangle$ values. As is obvious from the lack of $H\alpha$ emission in the $\langle dt \rangle = 2000$ -s run, no condensations were formed. The role of background heating is discussed further in §3.3.

The introduction of impulsive footpoint heating greatly enhances the dynamical behavior in the flux tube over that observed with steady heating. As can be seen easily by contrasting Fig. 1 with Figs. 2-5, sound waves are continually present in the impulsive-heating runs, not only varying the temperature and density but also affecting the position and size of any condensations. In some cases (e.g., Run 4) this helps delay or prevent the development of a long-lived, stationary condensation as is characteristic of all symmetric steady-heating runs.

3.2. Pulse duration variation

Two pulse durations, $\delta t = 20$ s and 200 s, were used to test the effects of heating impulsiveness on the plasma behavior. The detailed evolution of these cases diverges in several significant ways, although the overall trends are similar. Because condensations

always formed in the $\langle dt \rangle = 500$ -s runs, we confine our comparison to those cases. With heating scale $\lambda = 5$ Mm, the 200-s pulses produce the first condensation nearly 2 hrs earlier than do the 20-s pulses, and the accretion rate is much higher in the 200-s case. For example, both runs with background heating turned off yield a single condensation that grows at monotonically for 26 hrs, but the growth rate is nearly 50% faster for the 200-s pulses. It is more difficult to compare the runs with background heating: both form two condensations that coalesce and fall onto the chromosphere, then form additional pairs, but the relative timing is significantly different (see Figs. 2 and 3, or 7 and 8).

3.3. Background heating

The presence or absence of uniform background heating greatly influences the response of long flux tubes to footpoint heating. In particular, when the average interpulse interval is comparable to the radiative cooling time, condensations form without, but not with, background heating. The strong effect of background heating is best observed by comparing Runs 10 and 11 (Figs. 4 and 9) or 13 and 14 (see Figs. 6 and 10). Without background heating, the condensations also form earlier (see Figs. 1-3), by as much as 4 hours.

In order to clarify the effects of the background heating, it is important to distinguish physically between the $\langle dt \rangle = 2000$ -s runs and those with shorter interpulse intervals. For the cases with $\langle dt \rangle = 500$ s or less, which is substantially less than the radiative cooling time, the physics behind thermal nonequilibrium should apply, at least in a time-averaged sense. Note that condensation formation by thermal nonequilibrium is driven by the localization of the heating, not by its time dependence. If the heating were impulsive on a 500-s time scale (on average) but spatially uniform, the flux-tube plasma would achieve a time-averaged hot equilibrium with no condensation formation. Therefore, we expect that condensations will form in the short interpulse runs as long as the localized heating dominates the uniform background heating. Consequently the ratio of the total localized heating to the uniform background heating is a critical parameter. Equations (1) and (2) imply that the energy deposited in the flux tube by the uniform heating localized heating during one cycle is approximately 5 times that of the uniform heating — approximately the smallest value of this ratio for which thermal nonequilibrium still operates. Indeed, condensations do form in all of our simulations with a short interpulse interval, including the steady heating limit. In contrast, the ratio is infinite for runs with the background heating turned off, so thermal nonequilibrium is maximally effective.

The physical situation is quite different for the $\langle dt \rangle = 2000$ -s cases. Because 2000 s is of order the radiative cooling time, the evolution of these flux tubes is more akin to flare-loop

cooling than to thermal nonequilibrium in quasi-steady heated loops. Condensations form during flare-loop cooling due to a radiative instability mechanism in which perturbations in the initial temperature and density profiles grow faster than the loop as a whole cools (*e.g.*, Antiochos 1980). The condensations in this case tend to be smaller and have much shorter lifetimes than those produced by thermal nonequilibrium, which can last indefinitely and build up large mass (*e.g.*, Karpen *et al.* 2006). In fact, Figures 4 and 5 show that, when condensations do appear in the 2000-s runs, they are small, short-lived, and infrequent. This type of condensation resembles post-flare “loop prominences” or coronal rain rather than prominence components.

The uniform background heating suppresses condensation in the $\langle dt \rangle = 2000$ -s runs because it sets a lower limit on the density required for one to form. If this were the only heating in the flux tube, a condensation would never form; instead, the plasma would exhibit the well-known static-loop structure with a temperature maximum at the midpoint and with coronal temperature and density given by the usual scaling laws (Rosner, Tucker, & Vaiana 1978; Vesecky, Antiochos, & Underwood 1979):

$$Q_0 \approx 10^{-6} T_c^{7/2} / L^2 \approx n_c^2 \Lambda(T) \quad (3)$$

where T_c and n_c are the coronal temperature and density, L is the coronal flux-tube half-length (~ 140 Mm), and $\Lambda(T)$ is the radiative loss function (see Figure 1, Karpen *et al.* 2005). This yields the following solutions for T_c and n_c :

$$T_c \approx (10^{-6} Q_0 L^2)^{2/7} \approx 2.7 \text{ MK} \quad (4)$$

$$n_c \approx \left[\frac{10^{-6} T_c^{7/2}}{L^2 \Lambda(T_c)} \right]^{1/2} \approx 5.3 \times 10^8 \text{ cm}^{-3}. \quad (5)$$

The initial state of the numerical model, before the localized heating is added, is in good agreement with these estimates: $T_{max} = 2.9$ MK, and $n_{min} = 5.4 \times 10^8 \text{ cm}^{-3}$.

In order for a condensation to form, the density at some location in the flux tube far from the impulsive heating must rise substantially above the minimum value for a duration of order the cooling time. This situation never occurs when $\langle dt \rangle = 2000$ s. Instead, much of the extra material evaporated during each heating pulse drains out of the flux tube before cooling down to chromospheric temperatures. This result is evident from Figure 11, which shows the smoothed density at a specified coronal location for 2000-s runs with and without background heating (Runs 10 and 11). The densities have been filtered to remove short-lived spikes due to waves and initial evaporative flows. We note that the average density in Run 11 is well below that of Run 10, which is close to the minimum value derived above. This density reduction also is reflected in Figure 9, where the average baseline (excluding spikes)

Mg X intensity of Run 11 clearly is less than that of 10. Although condensations do form in Run 11, they form at densities far below the time-averaged density in Run 10. We conclude that the amount of persistent extra material injected into the flux tube by the impulsive heating is simply too small to trigger condensation formation when the background heating stays on.

3.4. Heating scale

The heating scale λ was reduced by a factor of 5 in Runs 3, 6, 9, 12, and 15, without altering the total heat input per pulse or the sum over the run. Even in the steady-heating calculation (Run 3), the shorter heating scale yields higher average temperatures outside the condensation, and the condensation forms ≤ 1 hr earlier than in either run with the longer λ . With impulsive heating the λ -dependent differences become more prominent, particularly for $\langle dt \rangle = 500$ s (Runs 6 and 9).

In the steady-heating cases, the minimum coronal density after the condensation has formed is approximately twice as high for Run 3 as for Run 1. With impulsive heating, the contrast in minimum coronal density is much smaller but still there; in addition, the wave-associated density spikes are significantly higher for the shorter heating scale. For both steady and impulsive heating, the baseline Mg X intensity is consistently higher when $\lambda = 1$ Mm (Figs. 6c-10c) compared with $\lambda = 5$ Mm (Figs. 6a-10a), to a lesser extent when no condensations are present (*e.g.*, Runs 13 and 15). The intensity range is greater as well with $\lambda = 1$ Mm for both O V and Mg X emissions, reflecting the stronger dynamics driven by heating pulses that are more spatially localized.

We expect more localized heating to produce higher densities, at least initially. If the heating pulse is very fast, radiative losses can be neglected and the impulsive energy deposited into the flux tube must go into creating a hot plasma. Hence

$$E_1 \sim n_1 T_1 L, \quad (6)$$

where E_1 is the total energy in a heating pulse, and n_1 and T_1 are the density and temperature of the resulting plasma. We use the maximum temperature produced by the heating pulse as an estimate for T_1 . When the pulse turns on, the local coronal temperature rises rapidly until the downward heat flux balances the instantaneous energy flux due to the impulsive heating:

$$E_1 / \delta t \sim T_1^{7/2} / \lambda, \quad (7)$$

where δt is the pulse duration as before. Substituting into the equation above we find that:

$$n_1 \sim E_1^{5/7} \delta t^{2/7} / (L \lambda^{2/7}). \quad (8)$$

Therefore, if we compare two heating pulses with the same total energy and duration but different deposition scales λ , the more localized pulse will produce a higher initial density. Our simulations are consistent with this relation.

3.5. Differential Emission Measure

Time-averaging the emission for each run essentially synthesizes the emission from a collection of flux tubes, as postulated by our prominence model. The instantaneous emission measure at each dump time was calculated from the density and length of each cell. The instantaneous emission measures per cell were then binned according to $\log_{10} T$, where each bin is 0.2 dex wide and $\log T$ is in the range 4.5-6.5; each bin was summed separately over the run and divided by the number of dumps to obtain the time-averaged DEM.

The most striking feature of the DEM plots is the systematic difference in shape between the runs that formed condensations and those that did not. Figures 12b and c show this difference most clearly, because condensations only formed in Runs 11 and 14. When condensations are present in the impulsive-heating calculations, the DEM has a broader, shallower minimum around 0.1 MK and decreases precipitously above $\log T=5.9$, whereas the condensation-free DEM has a deep minimum around $\log T=5.1$ and remains high at all coronal temperatures. The steady-heating DEMs (Figs. 11a and 12a) do not resemble any of the impulsive-heating DEMs, however, including those for Runs 4-9 (Fig. 11b and c).

We have compared these results with the few published DEMs derived from prominence observations. Kucera & Landi (2006) present column DEMs (cDEMs) over the range $\log T=5.0$ -6.2 for individual features in a prominence jet observed with the SUMER instrument on SOHO (see their Figs. 5 and 9), all of which exhibit a local minimum in the range $\log cDEM \sim 19 - 20$ around $\log T = 5.4$. Cirigliano, Vial, & Rovira (2004) derived a column DEM over the range $\log T=4.3$ -5.8 for a narrow slice of a prominence observed with SUMER and CDS/SOHO. Their cDEM plot qualitatively resembles the Kucera & Landi (2006) cDEMs but reaches a local minimum around $\log T = 5.3$ that is 0.3-1.3 dex higher than the minimum Kucera & Landi (2006) values. We can use our simulated volume DEM to estimate the effective length L_{eff} and filling factor f of plasmas at different temperatures from the observed column-DEM values, as follows:

$$L_{eff} = \frac{DEM_{sim}}{d \ cDEM_{obs}} \quad , \quad (9)$$

where the observed thread diameter $d \sim 10^7$ cm. At the local minimum in the DEMs, assumed to be at the same $\log T$ value for convenience, $DEM_{sim} \sim 10^{35}$ and $cDEM_{obs} \sim 10^{20}$

so $L_{eff} \sim 1$ Mm. At $\log T = 4.5$ (using the Cirigliano, Vial, & Rovira (2004) observations only), $L_{eff} \sim 100$ Mm, confirming that there is substantially more plasma in prominences at chromospheric than transition-region temperatures. If all of the plasma were in a single flux tube, then the corresponding filling factors, $f \sim L_{eff}/L_{cor}$, would be 0.3% and 30% respectively. However, the wispy appearance of most off-limb prominences suggests a much lower filling factor for cool material within the entire structure.

3.6. Condensation Velocity

One of the most striking differences between the steady and impulsive heating cases is in the condensation velocities. For steady heating (Runs 1-3), the condensation rapidly settles into a growing but quasi-stationary state, with small variations in the length of the condensation. Runs 1 and 2 exhibit little if any displacement of the center of mass from the flux tube midpoint, once the initial pair of condensations has coalesced. In the case with $\lambda = 1$ Mm (Run 3), however, the center of mass also oscillates around the midpoint of the flux tube from birth until the end of the calculation; the period is approximately 3 hours, while the amplitude of the oscillation grows slowly, reaching ~ 3 Mm in 24 hours. With impulsive heating, both fully dynamic and quasi-stationary condensations are formed, as well as coalescing pairs (Karpen *et al.* 2006). Figure 13 shows the center of mass location vs time for Runs 4, 6, and 11. Simple linear fits to the slopes of these plots, excluding periods when the condensation reverses direction, yield speeds in the ranges 6-31 km s^{-1} (Run 4), 5-29 km s^{-1} (Run 6), and 20-115 km s^{-1} . Values for the analogous $\delta t = 200$ s runs are comparable, including the increased speeds for $\langle dt \rangle = 2000$ s with no background heating.

4. Conclusions

Our simulations demonstrate that condensations can form through thermal nonequilibrium in long, low-lying flux tubes with impulsive random heating localized above the chromosphere. For average intervals between heating pulses less than the coronal radiative cooling time, condensations form readily under the variety of circumstances tested here. For intervals comparable to or greater than the radiative cooling time, however, condensations only form when there is no background heating in the flux tube.

One-dimensional calculations of time-dependent plasma behavior in response to impulsive heating just above the chromosphere were reported recently by Testa *et al.* (2005) and Mendoza-Briceño & Erdélyi (2006), for semi-circular flux tubes representing typical coronal

loops of vastly different lengths (200 Mm and 10 Mm, respectively). These studies are not directly comparable to the prominence-oriented work discussed here, because of fundamental differences in the assumed symmetries, heating pulse characteristics, and boundary conditions. However, they also find that coronal condensations can be generated by impulsive, localized footpoint heating, with and without uniform background heating, when the pulse duty cycle is less than the radiative cooling time.

In particular, we find distinct, observable differences from the results of steady footpoint heating. The mass of each condensation is significantly greater for the steady heating case. As one might expect, impulsive heating produces a much more dynamic system, with more variations in speed and direction, ever-present waves, and some falling condensations despite the time-averaged symmetry of the energy input. The time-averaged differential emission measures also depend on the time variability of the heating, although in all cases the presence or absence of prominence material can be deduced from the shape of the DEM. More observations over a wider temperature range, as could be obtained by EIS/Hinode, are needed to fully characterize the DEM of both active-region and quiescent prominences, in order to estimate the total cool mass in the majority of prominences for which only limited spectral coverage is available. The motions produced by impulsive heating vary from case to case, but in general the condensation moves back and forth in each flux tube with speeds from 5 - 30 km s⁻¹. This provides a natural explanation for the observed counterstreaming flows, without requiring significant variations in the footpoint heating rate on adjoining flux tubes as in our asymmetric steady-heating simulations (*e.g.*, Karpen *et al.* 2001).

Our extensive studies of thermal nonequilibrium have shown that a wide range of observed condensation properties can be produced by this process in flux tube geometries typical of the sheared arcade configuration, by either steady and impulsive heating just above the chromosphere. These properties include subsonic counterstreaming flows as well as stationary condensations; small knots as well as long threads; and occasional higher speed flows comparable to those derived from EUV observations (Kucera, Tovar, & De Pontieu 2003). Our results place important constraints on the coronal heating properties in filament channels, if thermal nonequilibrium is indeed the process responsible for the cool, dense threads and knots comprising a prominence. To date this is the only mechanism that explains the frequent observation of cool prominence elements appearing abruptly in the corona without evidence of direct levitation or injection from below. Tests of thermal nonequilibrium in other models of prominence magnetic structure, and comparably quantitative investigations of alternative theories for the origins of prominence plasma, are urgently needed if we are to make progress in understanding solar activity.

This work has been supported in part by the NASA Solar Physics SR&T program and

ONR. We thank the PROM team, Enrico Landi, Jim Klimchuk, and Spiros Patsourakos for lively and informative discussions.

REFERENCES

- Antiochos, S. K. 1980, *ApJ*, 236, 270
- Antiochos, S. K. & Klimchuk, J. A. 1991, *ApJ*, 378, 372
- Antiochos, S. K., Dahlburg, R. B. & Klimchuk, J. A. 1994, *ApJ*, 420, L41
- Antiochos, S. K., MacNeice, P. J., Spicer, D. S., & Klimchuk, J. A. 1999, *ApJ*, 512, 985
- Antiochos, S. K., Karpen, J. T., DeLuca, E. E., Golub, L., & Hamilton, P. 2003, *ApJ*, 590, 547
- Antiochos, S. K., MacNeice, P. J., & Spicer, D. S. 2000, *ApJ*, 536, 494
- Anzer, U., & Heinzel, P. 2003, *A&A*, 404, 1139
- Aschwanden, M., Schrijver, C.J., & Alexander, D. 2001, *ApJ*, 550, 1036
- Aulanier, G., DeVore, C.R., & Antiochos, S.K. 2002, *ApJ*, 567, L97
- Aulanier, G., and Schmieder, B. 2002, *A&A*386, 1106
- Boris, J. P. , & Mariska, J. T. 1982, *ApJ*, 258, L49
- Brekke, P., Kjeldseth-Moe, O., & Harrison, R. A. 1997, *Sol. Phys.*, 175, 511
- Chae, J., Denker, C., Spirock, T. J., Wang, H., & Goode, P. R. 2000, *Sol. Phys.*, 195, 333
- Chae, J. 2003, *ApJ*, 584, 1084
- Cirigliano, D., Vial, J.-C., & Rovira, M. 2004, *Sol. Phys.*, 223, 95
- Craig, I. J. D., & McClymont, A. N. 1986, *ApJ*, 307, 367
- Dahlburg, R. B., Antiochos, S. K., & Klimchuk, J. A. 1998, *ApJ*, 495, 485
- Devore, C. R., & Antiochos, S. K. 2000, *ApJ*, 539, 954
- Engvold, O. 2004, *Proceedings of the IAU Vol. 2004, No IAUS223*,187
- Foullon, C., Verwichte, E., & Nakariakov, V. M. 2004, *A&A*, 427, L5

- Karpen, J. T., Antiochos, S. K., Hohensee, M., Klimchuk, J. A., & MacNeice, P. J. 2001, ApJ, 553, L85
- Karpen, J. T., Antiochos, S. K., Klimchuk, J. A., & MacNeice, P. J. 2003, ApJ, 593, 1187
- Karpen, J. T., Antiochos, S. K., Tanner, S. E., & DeVore, C. R. 2005, ApJ, ApJ 635, 1319
- Karpen, J. T., Antiochos, S. K., & Klimchuk, J. A. 2006, ApJ, 637, 531 [Paper 4]
- Klimchuk J.A., 2006, Sol. Phys., 234, 41
- Klimchuk, J. A., & Cargill, P. J. 2001, ApJ, 553, 440
- Kucera, T. A., Tovar, M., & De Pontieu, B. 2003, Sol. Phys., 212, 81
- Kucera, T. A., & Landi, E. 2006, ApJ, 645, 1525
- Lin, Y., Engvold, O., & Wiik, J. E. 2003, Sol. Phys., 216, 109
- Mariska, J. T., & Boris, J. P. 1983, ApJ, 267, 409
- Martin, S. F., & Echols, C. R. 1994, in Solar Surface Magnetism, eds. R.J. Rutten & C. J. Schrijver (Dordrecht: Kluwer), 339
- Mendoza-Briceño, C. A., Sigalotti, L. d. G., & Erdélyi, R. 2005, ApJ, 624, 1080
- Mendoza-Briceño, C. A., & Erdélyi, R. 2006, ApJ, 648, 722
- Mok, Y., Drake, J. F., Schnack, D. D., & Van Hoven, G. 1990, ApJ, 359, 228
- Müller, D. A. N., Hansteen, V. H., & Peter, H. 2003, A&A, 411, 605
- Müller, D. A. N., De Groof, A., Hansteen, V. H., & Peter, H. 2005, A&A, 436, 1067
- Patsourakos, S., Klimchuk, J. A., & MacNeice, P. J. 2004, ApJ, 603, 322
- Pécseli, H., & Engvold, O. 2000, Sol. Phys., 194, 73
- Dynamic and Structure of Quiescent Solar Prominences*, ed. E.R. Priest (Dordrecht: Kluwer)
- Priest, E. R., Hood, A. W., & Anzer, U. 1989, ApJ, 344, 1010
- Rosner, R., Tucker, W. H., & Vaiana, G. S. 1978, ApJ, 220, 643
- Schmieder, B., Rust, D. M., Georgoulis, M. K., Démoulin, P., & Bernasconi, P. N. 2004, ApJ, 601, 530

- Schrijver, C. J. 2001, *Sol. Phys.*, 198, 325
- Serio, S., Peres, G., Vaiana, G. S., Golub, L., & Rosner, R. 1981, *ApJ*, 243, 288
- Stineman, R. W. 1980, A consistently well-behaved method of interpolation. *Creative Computing*, July 1980.
- Testa, P., Peres, G., & Reale, F. 2005, *ApJ*, 622, 695
- Van Ballegooijen, A. A., & Martens, P. C. H. 1990, *ApJ*, 361, 283
- Vesecky, J. F., Antiochos, S. K., & Underwood, J. H. 1979, *ApJ*, 233, 987
- Vourlidas, A., & Korendyke, C. 2004, AAS/SPD meeting #34, #20.09
- Warren, H., Winebarger, A. R., & Mariska, J. T. 2003, *ApJ*, 593, 1174
- Zirker, J. B., Engvold, O., & Martin, S. F. 1998, *Nature*, 396, 440

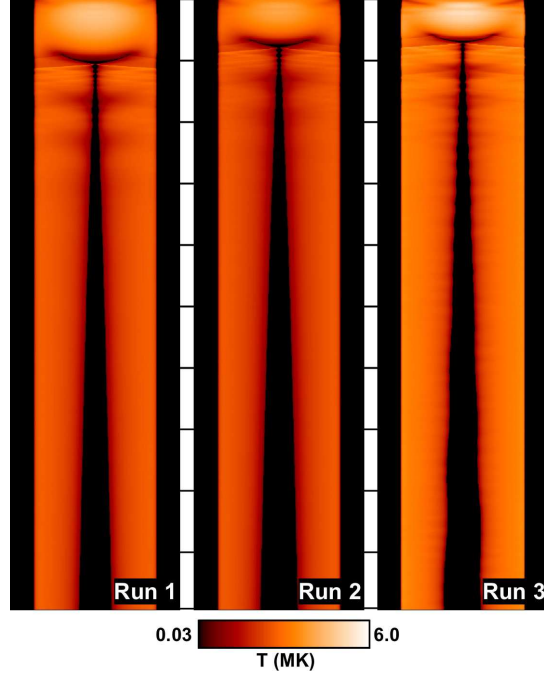


Fig. 1.— Temperature along the flux tube during Runs 1 (left), 2 (middle), and 3 (right). In each strip plot, distance along the flux tube runs from left to right, while time runs from top to bottom. The black bars between the 3 plots are spaced 10^4 s apart. The same color scale is used for Figs. 2-5.

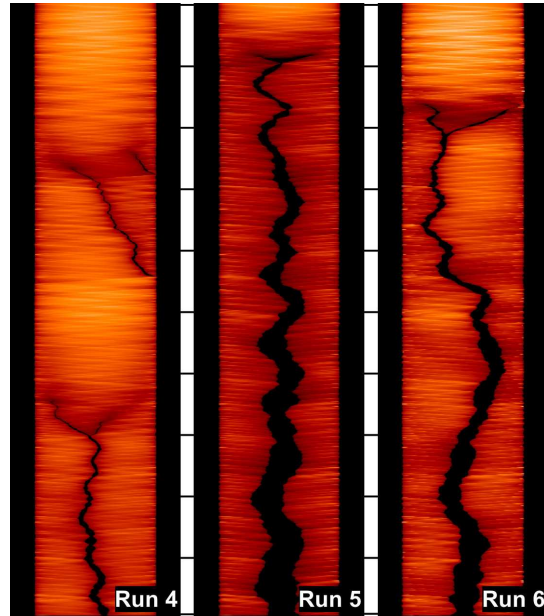


Fig. 2.— Same as Fig. 1 for Runs 4, 5, and 6 .

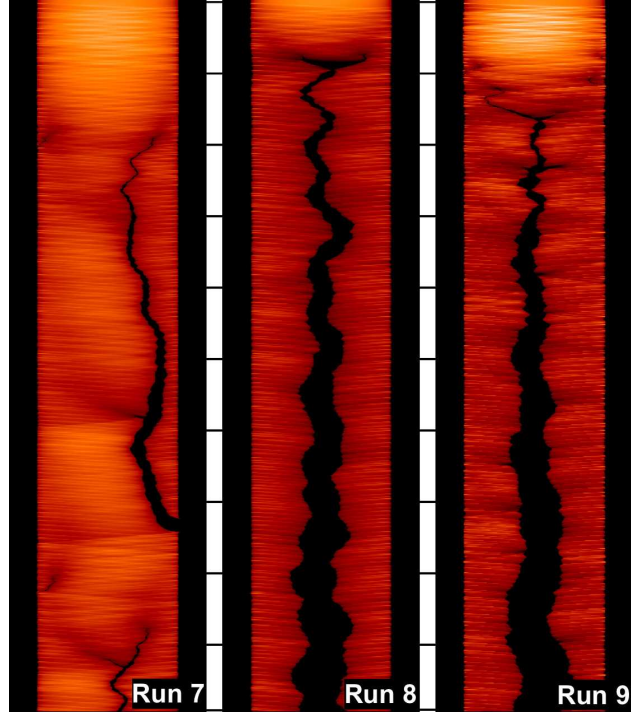


Fig. 3.— Same as Fig. 1 for Runs 7, 8, and 9.

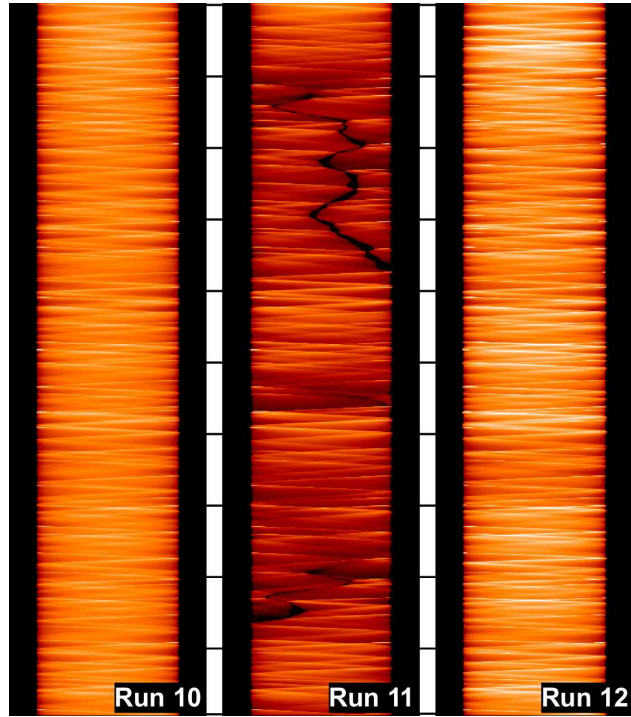


Fig. 4.— Same as Fig. 1 for Runs 10, 11, and 12.

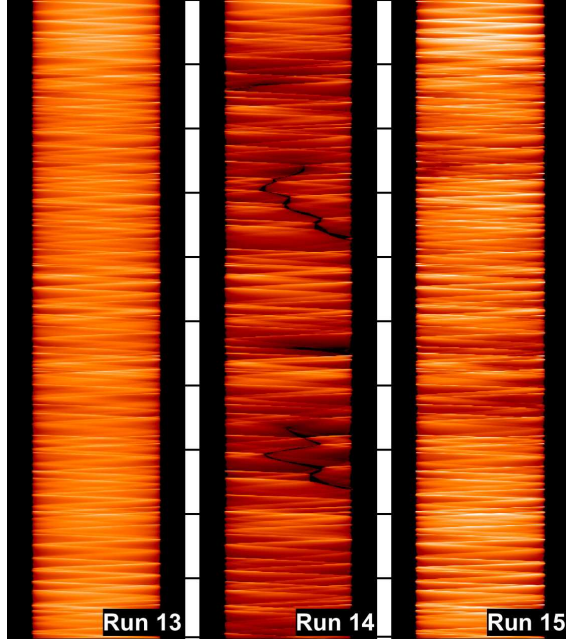


Fig. 5.— Same as Fig. 1 for Runs 13, 14, and 15.

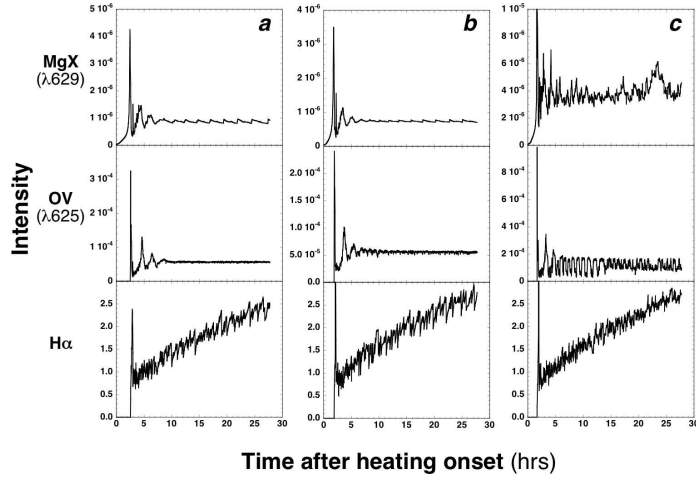


Fig. 6.— Time evolution of predicted $H\alpha$ (*bottom*), $O\ V$ ($629\ \text{\AA}$) (*middle*), and $Mg\ X$ ($625\ \text{\AA}$) (*top*) spatially integrated emission intensities. Plasma at $T < 35000\ \text{K}$ was simply assumed to be producing $H\alpha$ emission, on an arbitrary intensity scale because radiative transport has not been included. The $O\ V$ and $Mg\ X$ intensities are computed for each grid point in an infinitely thin flux tube, modulated by the instrument response function for the SOHO CDS instrument (see earlier papers for details), summed over the coronal portion of each flux tube ($s = 65 - 340\ \text{Mm}$) to avoid the intense stationary component around each footpoint. (*a*) Run 1. (*b*) Run 2. (*c*) Run 3.

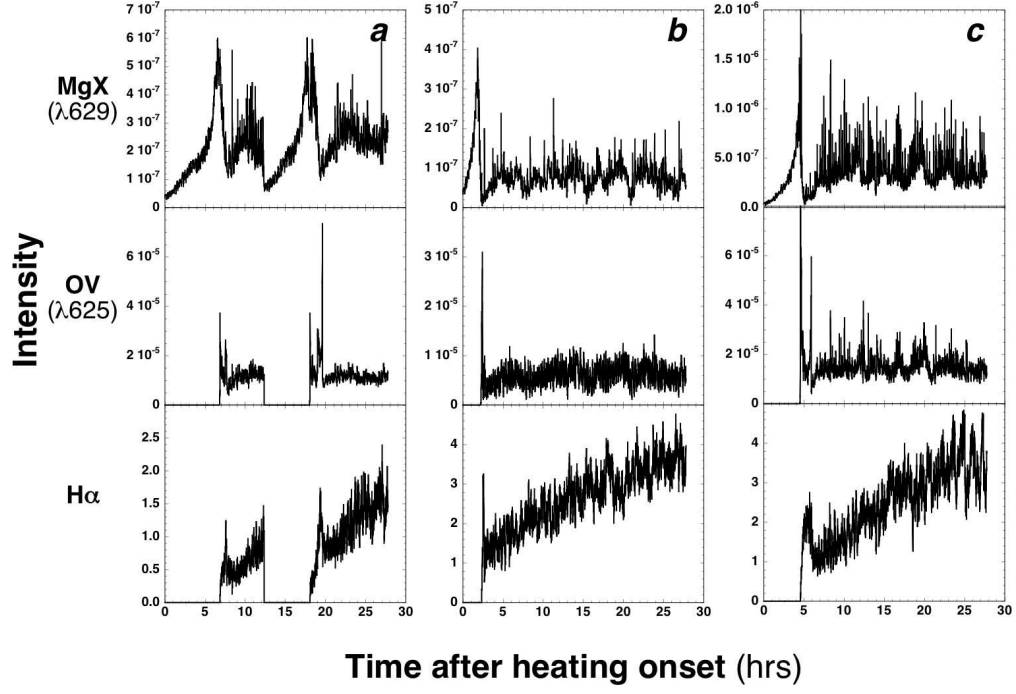


Fig. 7.— Same as Fig. 6 for Runs 4, 5, and 6.

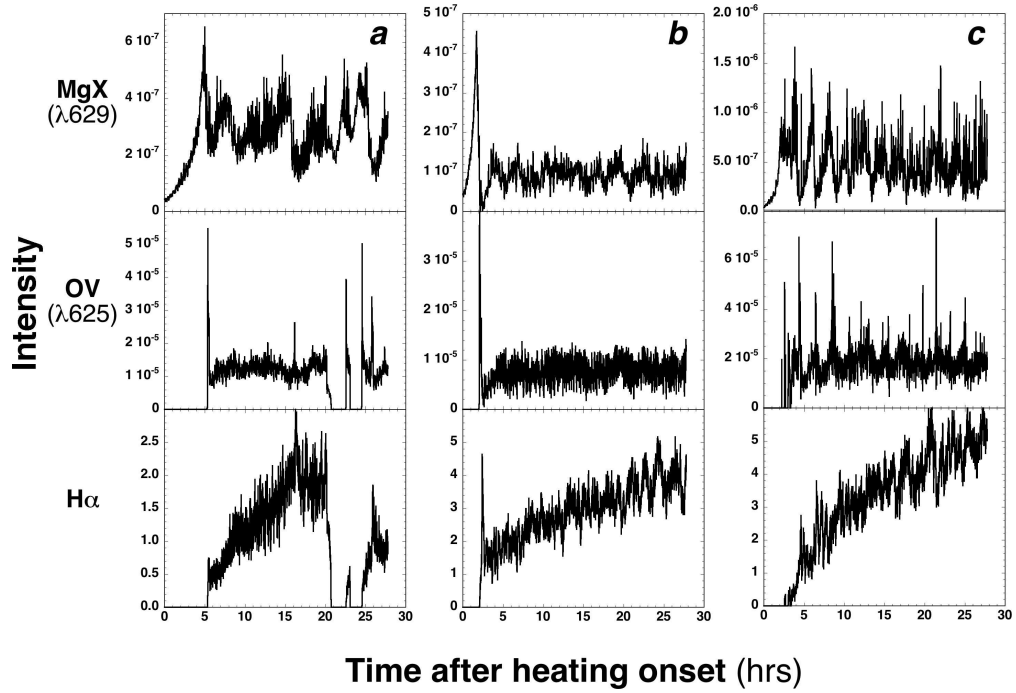


Fig. 8.— Same as Fig. 6 for Runs 7, 8, and 9.

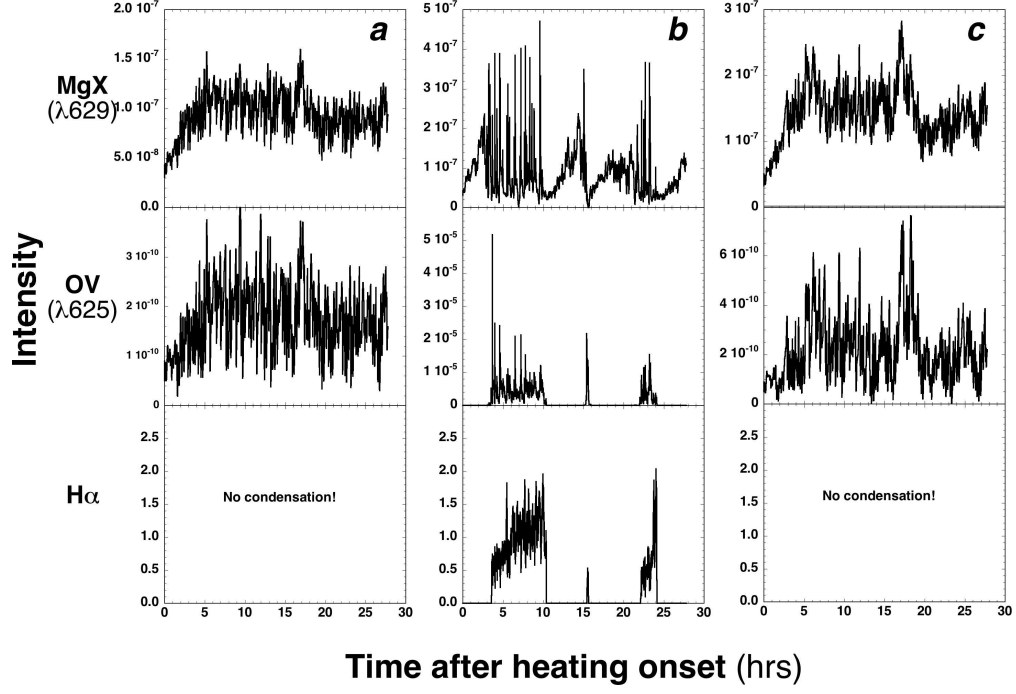


Fig. 9.— Same as Fig. 6 for Runs 10, 11, and 12.

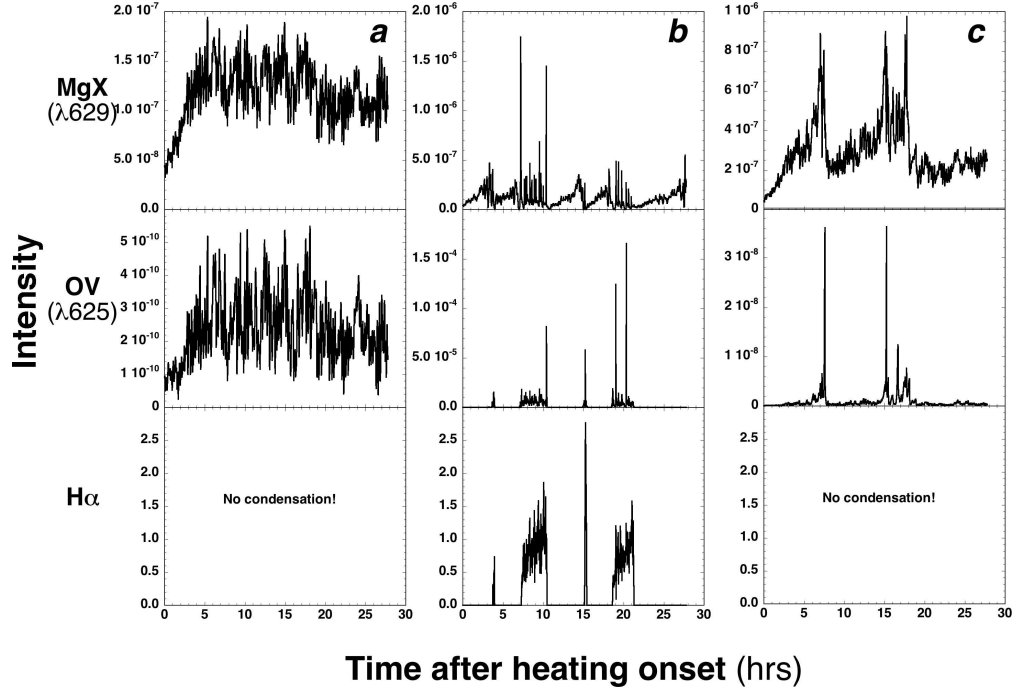


Fig. 10.— Same as Fig. 6 for Runs 13, 14, and 15.

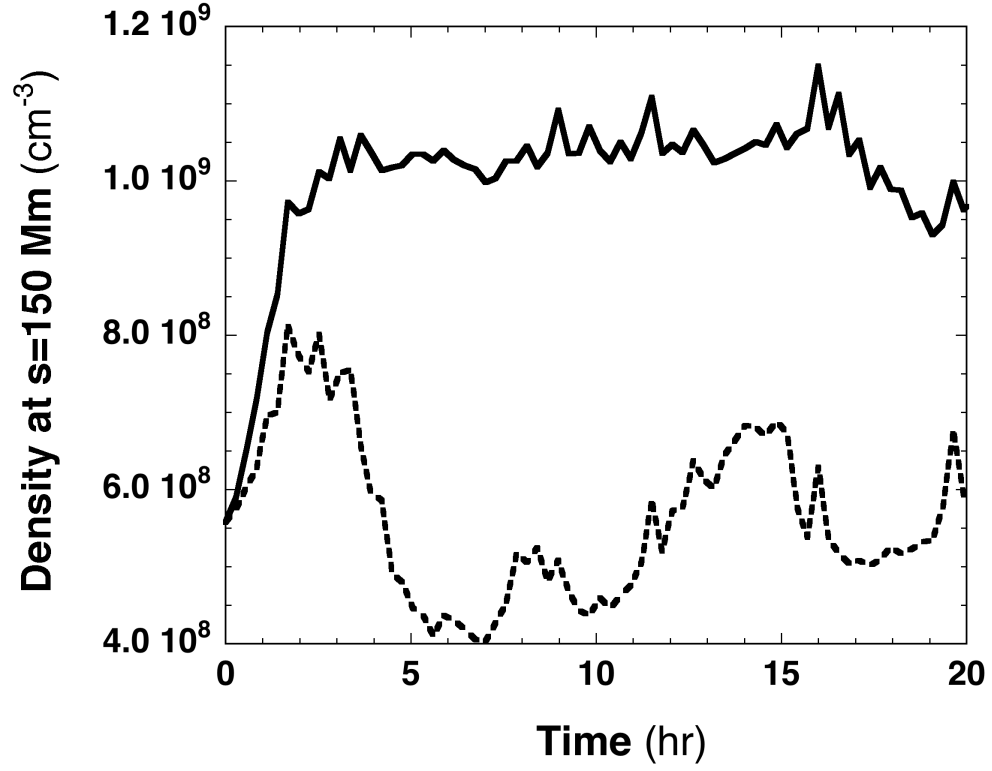


Fig. 11.— Density at $s = 150$ Mm vs. time during Runs 10 (solid line) and 11 (dashed line). The densities have been smoothed by a Stineman function (Stineman 1980), which removes high-frequency spikes that would otherwise bias the average away from the baseline values.

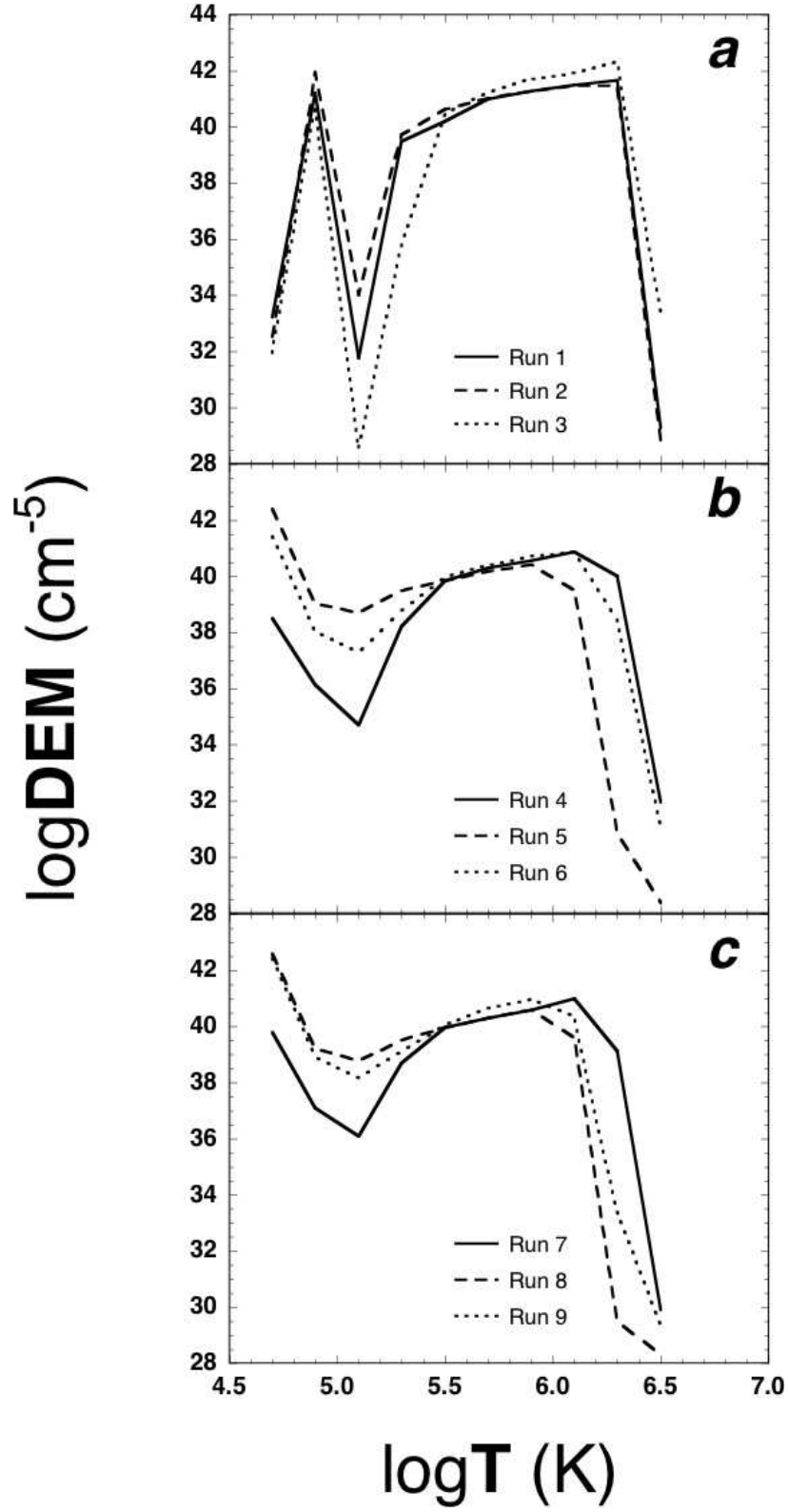


Fig. 12.— Time-averaged differential emission measures vs. temperature. *a*) Runs 1-3. *b*) Run 4-6. *c*) Runs 7-9.

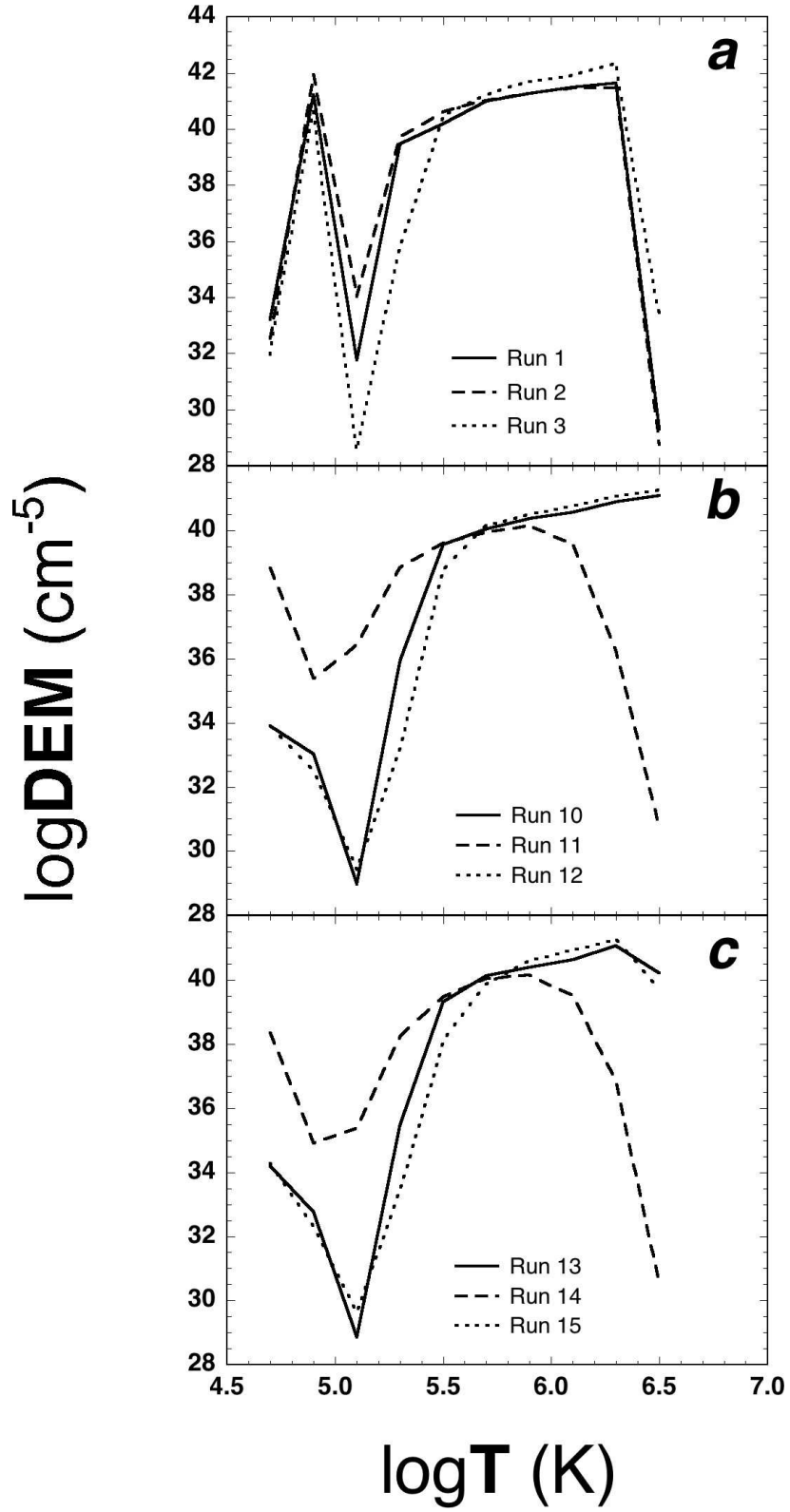


Fig. 13.— Time-averaged differential emission measures vs. temperature. *a*) Runs 1-3. *b*) Runs 10-12. *c*) Runs 13-15.

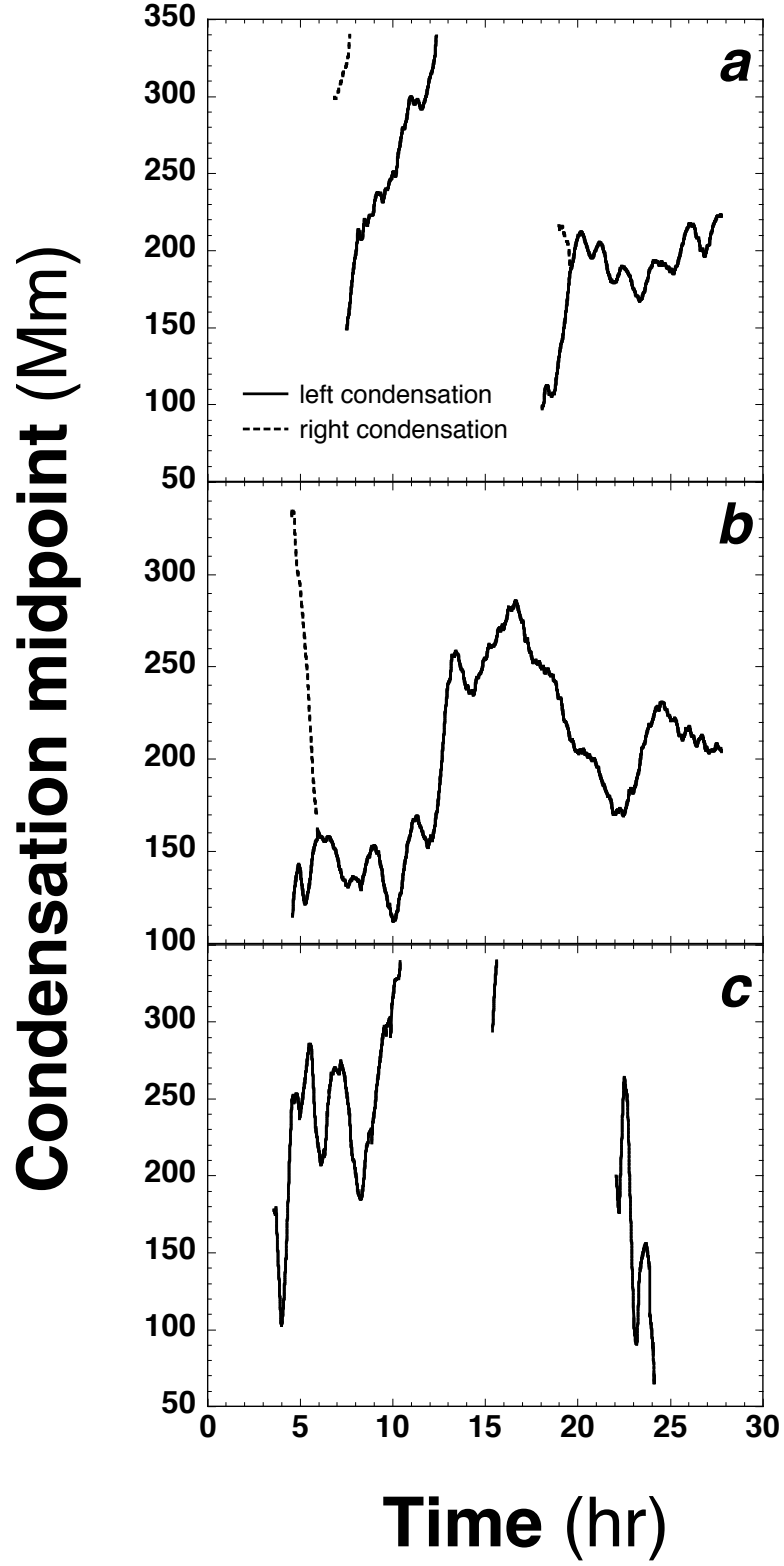


Fig. 14.— Condensation midpoint location vs. time. *a*) Run 4. *b*) Run 6. *c*) Run 11.

Table 1. Simulation Parameters

Run	Median Interpulse Interval (s)	Pulse Duration (s)	Background heating on	λ (Mm)
1	0	inf	yes	5
2	0	inf	no	5
3	0	inf	yes	1
4	500	20	yes	5
5	500	20	no	5
6	500	20	yes	1
7	500	200	yes	5
8	500	200	no	5
9	500	200	yes	1
10	2000	20	yes	5
11	2000	20	no	5
12	2000	20	yes	1
13	2000	200	yes	5
14	2000	200	no	5
15	2000	200	yes	1

Note. — See text for initial and boundary conditions common to all simulations.